HiSST: 3rd International Conference on
High-Speed Vehicle Science Technology
14 -19 April 2024, Busan, Korea

A Contribution to Mitigate NO_x and H_2O Emissions for a Hydrogen-Powered Hypersonic Vehicle

Daniel Bodmer[1], Jacob Jäschke[2], Florian Linke[3] and Volker Gollnick[4]

Abstract

Hypersonic transport fueled with liquid hydrogen (LH_2-HST) is currently considered as long-term future technology of civil aviation to fly with speeds greater than Mach 5 at stratospheric altitudes of 25-38 km. In this paper, we present a comprehensive methodology to assess the emission mitigation potential (via NO_x and H_2O) of future LH_2-HST through operational measures, considering realistic constraints such as the sonic boom carpet as well as tolerable g-forces acting on the passengers while flying with hypersonic speeds. Both NO_x- and H_2O-optimal 4D-trajectories are identified by a brute-force algorithm that varies the initial cruise altitude from 30 km to 36 km. As case study, the Mach 8 passenger aircraft STRATOFLY-MR3, which was conceptually developed in the framework of the H2020 STRATOFLY project, is operated on a single route from Brussels (BRU) to Sydney (MYA). The findings are highlighted as relative changes regarding MR3's design flight altitude set at 32 km, respectively 105 000 ft. As scientific contribution, 3D emission inventories are calculated and made publicly available for a world fleet of MR3 aircraft operated along the BRU-MYA route on both NO_x- and H_2O-optimal mission profiles in the year 2075.

Keywords: *Hypersonic Transport, Emission Mitigation Potential, 4D-Trajectories, HTCM, STRATOFLY, MORE&LESS*

Nomenclature

ATC	Air Traffic Control
ATR	Air Turbo Rockets
CAS	Calibrated Airspeed
CCC	Continuous Climb Cruise
CIMP	Climate Impact Mitigation Potential
CoG	Center of Gravity
DLR	German Aerospace Center
DMR	Dual Mode Ramjet
EC	European Commission
EIS	Entry into Service
EQMP	Emission Quantity Mitigation Potential
FPMM	Flight-Path Modification Module
H_2O	Water Vapour
HST	Hypersonic Transport
HTCM	Hypers. Trajectory Calculation Module
ICA	Initial Cruise Altitude
ILT	Institute of Air Transportation Systems
LH_2	Liquid Hydrogen
MR3	Manta Ray 3
MTOW	Maximum Take-Off Weight
NO_x	Nitrogen Oxides
PI	Proportional-Integrating
RF	Radiative Forcing
SB	Sonic Boom
SST	Supersonic Transport
TAS	True Airspeed
TCM	Trajectory Calculation Module
TUHH	Hamburg University of Technology
WP	Waypoint

[1] Institute of Air Transportation Systems (ILT), Hamburg University of Technology, daniel.bodmer@tuhh.de
[2] Institute of Air Transportation Systems (ILT), Hamburg University of Technology, jacob.jaeschke@tuhh.de
[3] Institute of Air Transport, German Aerospace Center (DLR), florian.linke@dlr.de
[4] Institute of Air Transportation Systems (ILT), Hamburg University of Technology, volker.gollnick@tuhh.de

1. Introduction

The era of hypersonic flight dawned on June 23, 1963, when Robert White was the first person to reach a hypersonic flight speed of Mach 5.24 as part of the *North American X-15* flight program ([1]). From that day on, a significant impetus to consider commercial HST is spurring Europe to conduct a thorough assessment [2]-[9] of the potential for civil high-speed aviation with regard to environmental, technical and economic viability, along with aspects related to human factors, social acceptance and operational measures. HST could revolutionize long-haul air travel primary through a major reduction in flight times, especially for antipodal routes, and secondary by "decarbonizing" air transport within Europe due to the use of new high-speed propulsion systems powered by post-fossil, renewable fuels like green hydrogen, whose overall CO_2-balance is considered neutral in the biogenic carbon cycle (see e.g. [10]-[12]).

The pursuit of zero CO_2-emissions and flight time reductions by one order of magnitude have led to the development of a novel aircraft concept named STATOFLY-MR3, which is shown in Fig 1.

However, the realization of HST as a future concept may face considerable obstacles from an operational and climatological point of view: As per [13], the contribution of high-altitude (stratospheric) emissions to the effective radiative forcing primarily depends on non-CO_2 effects such as water vapour (H_2O) and nitrogen oxides (NO_x), with H_2O being identified as the key climate driver due to is large residence time of ~3-4 years. Given that the time, quantity, and geographical location (longitude, latitude, altitude) of an emission contribute to climate impact in varying proportions, operational measures are needed which

(i) reduce the total amount of emissions emitted along the aircraft's flight trajectory by optimizing its 3D flight profile through an adaption of the flight altitude h, respectively ICA;
(ii) guarantee that specific operating constraints during the mission are not violated.

These constraints come from (ii-1) the current regulatory framework for civil supersonic transport (SST) and HST alongside (ii-2) the passenger comfort when flying at speeds greater than Mach 5: On the one hand, en-route noise emissions in the form of a sonic boom are emitted by the aircraft when it surpasses Mach 1 forming a *sonic boom carpet* [14] on ground that makes overland SST/HST impossible due to prevailing international noise regulations as § 91.817 in CFR Title 14 [15]. Hence, only water dominated routes can be considered for HST limiting the beneficial location (longitude λ, latitude φ) of an emission with respect to climate impact. On the other hand, anthropometric passenger g-forces - that have been adjusted to tolerable loads on the passengers' musculoskeletal system - are necessary to comply with a realistic flight routing leading to large turn radii as well as long deceleration and acceleration phases. For instance, a hypersonic cruise speed of Mach 8 yields a substantial turn radius reaching up to 905 km to ensure a normal load factor of $n_z = 1.2$. Consequently, executing even a modest course adjustment, such as $\Delta\chi_K = 10°$, requires more than 1 min of flight time, posing considerable operational challenges for hypersonic flight missions that are addressed in this work.

1.1. The EU Research Project STRATOFLY

From June 2018 to May 2021 the *Stratospheric Flying Opportunities for High-Speed Propulsion Concepts* (STRATOFLY) project has been funded by the EC, under the framework of the Horizon 2020 Program. One of the main project goals relates to the conceptual design and revision of the hypersonic passenger aircraft STRATOFLY-MR3 [16] (see Fig 1), which is an enhanced waverider configuration of the design base LAPCAT-MR2.4 [17] being developed in previous EC funded projects LAPCAT I/II.

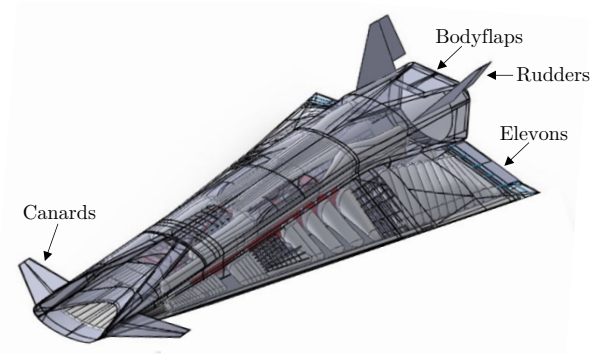

Fig 1. Hypersonic passenger aircraft STRATOFLY-MR3 (structural layout)

With a maximum take-off weight (MTOW) of 410 446 kg, the primary objective of MR3 is to convey 300 passengers (33 000 kg) over 18 520 km (10 000 nm) at a speed of Mach 8 maintaining a cruise altitude of 32 km (105 000 ft) using 181 250 kg of liquid hydrogen (LH_2) as fuel. Due to the large range and high-speed requirements, the LH_2-powered propulsion system is designed according to the ascent trajectory and consists of six air turbo rockets (ATR) and a dual mode ramjet (DMR) engine. The ATR/DMR engines are arranged coaxially and share the same elliptical air intake and thrust nozzle ([18]).

1.2. Methodology for Environmental Analysis of Civil High-Speed Aircraft

As a corollary to the previous section, the future goal of revolutionizing long-haul air travel through LH_2-HST requires a multi-disciplinary model approach that satisfies (i) and (ii) including (ii-1) and (ii-2) with a high level of detail to assess the potential of novel HST configurations being operated at flight profiles with a reduced amount of gaseous engine emissions. Such a comprehensive approach was developed by the *Institute of Air Transportation Systems* (ILT) at *Hamburg University of Technology* (TUHH) using a holistic simulation tool chain (see Fig 2) that incorporates:

- The *Hypersonic Trajectory Calculation Module* (HTCM) as mission simulator to calculate high-fidelity 4D-trajectories;
- A ray tracing algorithm to estimate primary sonic boom carpets along the aircraft's flight path, considering real weather data including winds;
- An emission model that determines the quantity and distribution of gaseous engine emissions;
- An algorithm that generates a noise-optimal flight path based on operational changes in route waypoints (2D trajectory optimization)
- An algorithm that produces an emission-optimal flight profile based on operational changes in cruise altitude (1D trajectory optimization)
- The *Global Air Traffic Emission Distribution Laboratory* (GRIDLAB) [19] that rasterizes emission profiles into a 3D discrete spatial and temporal coordinate grid;
- A hypersonic airline network [9] with respect to HST passenger demand.

These software tools and models are interconnected within MATLAB through an iterative procedure to identify the emission quantity mitigation potential (EQMP) of civil hypersonic passenger aircraft ensuring meaningful, comparable, and reliable results. For this paper, the simulation chain is applied to the MR3 vehicle to reveal the $EQMP_{NO}$ and $EQMP_{H2O}$ in relation to its design flight altitude of 32 km (105 000 ft).

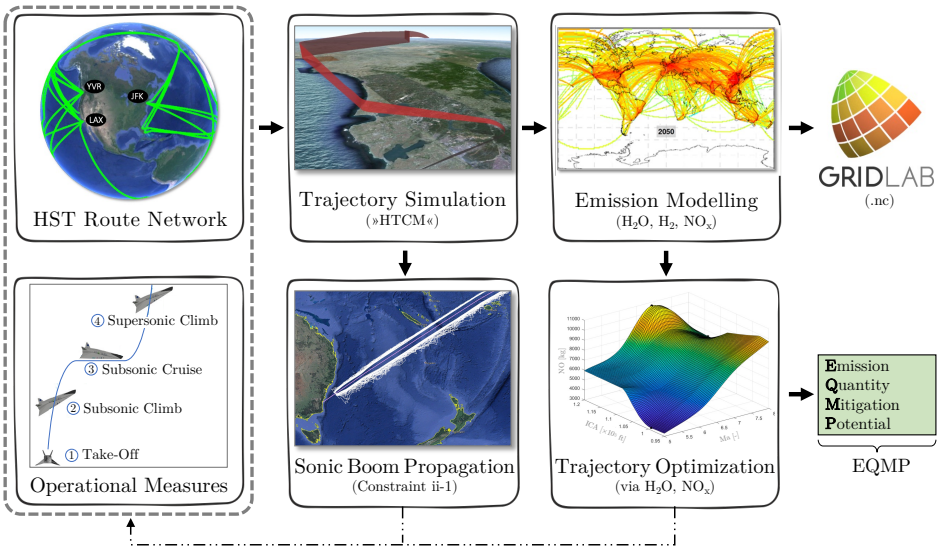

Fig 2. Methodology for environmental assessment of hypersonic air transportation systems

1.3. Outline

The remainder of this paper is organized as follows: Section 2 provides an overview of the HTCM along with the emission model, followed by the description of the sonic boom carpet determination algorithm in Section 3. Section 4 elaborates on the trajectory optimization algorithms. Section 5 outlines the results of applying the methodology for environmental analysis of HST, including the 3D emission inventories. Finally, the paper concludes with a summary and highlights future research directions.

2. Hypersonic Trajectory Calculation Module (HTCM)

To precisely determine 4D-trajectories, which represent the physical space curve (3D) along which the aircraft moves as a function of time (1D), the software tool HTCM[5] is utilized. This tool simulates the aircraft's movement from lift-off to touch-down based on a nonlinear 3-degree-of-freedom (3DOF) point mass model in which the differential equations of motion are solved numerically using the *Euler method,* while incorporating processed flight performance data from the aerodynamic and engine characteristics. The aircraft dynamics are affected by a direct thrust force control $F_{\mathrm{TW,c}} \in \mathbb{R}$ as well as a virtual control input vector $\vec{u} = \left[\tau_{\dot{V}},\ \tau_{\dot{\chi}},\ \tau_{\dot{\gamma}},\ \tau_{\dot{\mu}}\right] \in \mathbb{R}^4$, which results from the linear feedback laws of the state control loops; both contributing to the nonlinear simulation of the controlled hypersonic vehicle. The computed 4D-trajetory contains the complete history of the aircraft state vector $\vec{x} = [V, \chi, \gamma, \mu, \lambda, \varphi, h, m]^{\mathrm{T}} \in \mathbb{R}^7$, where V represents the fight-path velocity, χ the flight-path azimuth angle, γ the flight-path inclination angle, μ the flight-path bank angle, λ the longitude, φ the geocentric latitude, h the geometric altitude, and m the aircraft's mass, but also all state variables that collectively describe the overall HTCM model state at any given point in time, such as e.g. the load factor n_z or the ambient temperature T.

Within the HTCM, particular emphasis was placed on a detailed modelling of the intricate mechanics of hypersonic flight on the one hand, which causes distinct phenomena that are not present in conventional aircraft such as fictitious forces due to the curvature of Earth (Term ✯; Eq. 4), and a sufficient numerical calculation accuracy on the other hand that enables a realistic implication of the quantity and distribution of high-altitude emissions for a single mission, which can subsequently be scaled to a global fleet level.

2.1. Nonlinear Differential Equations of Motion for Hypersonic Aircraft

According to [21], the movement of a hypersonic aircraft, approximated as point mass, over a spherical, rotating earth can be expressed by the following nonlinear differential equations:

$$\dot{V} = \frac{F_{\mathrm{TW,c}} \cdot \cos\alpha - D}{m} - g \cdot \sin\gamma - {\omega_{\mathrm{E}}}^2 \, (r_{\mathrm{E}} + h) \, \cos\varphi \cdot \left[\cos\gamma \cdot \cos\chi \cdot \sin\varphi - \sin\gamma \cdot \cos\varphi\right]$$

$$\dot{\chi} = \frac{F_{\mathrm{TW,c}} \cdot \sin\alpha + L}{m \cdot V \cdot \cos\gamma} \cdot \sin\mu + \left[\tan\gamma \cdot \cos\chi \cdot \dot{\lambda} \cdot \cos\varphi - \tan\gamma \cdot \sin\chi \cdot \dot{\varphi} - \dot{\lambda} \cdot \sin\varphi\right] - 2 \cdot \omega_{\mathrm{E}} \cdot \left[\tan\gamma \cdot \cos\chi \cdot \cos\varphi - \sin\varphi\right] + \frac{{\omega_{\mathrm{E}}}^2 (r_{\mathrm{E}} + h)}{V \cdot \cos\gamma} \cdot \left[\sin\chi \cdot \sin\varphi \cdot \cos\varphi\right] \quad (1)$$

$$\dot{\gamma} = \frac{F_{\mathrm{TW,c}} \cdot \sin\alpha + L}{m \cdot V} \cdot \cos\mu + 2 \cdot \omega_{\mathrm{E}} \cdot \sin\chi \cdot \cos\varphi - \frac{g}{V} \cdot \cos\gamma + \left[\sin\chi \cdot \dot{\lambda} \cdot \cos\varphi + \cos\chi \cdot \dot{\varphi}\right] + \frac{{\omega_{\mathrm{E}}}^2 (r_{\mathrm{E}} + h)}{V} \cdot \cos\varphi \left[\sin\gamma \cdot \cos\chi \cdot \sin\varphi \cdot + \cos\gamma \cdot \cos\varphi\right]$$

$$\dot{\varphi} = \frac{V \cdot \cos\gamma \cdot \cos\chi}{(r_{\mathrm{E}} + h)}$$

$$\dot{\lambda} = \frac{V \cdot \cos\gamma \cdot \sin\chi}{(r_{\mathrm{E}} + h) \cdot \cos\varphi}$$

$$\dot{h} = -V \cdot \sin\gamma$$

$$\dot{m} = -\dot{m}_{\mathrm{TW}}$$

with

$$g = g_0 \cdot \left(\frac{r_{\mathrm{E}}}{r_{\mathrm{E}} + h}\right)^2 \quad (2)$$

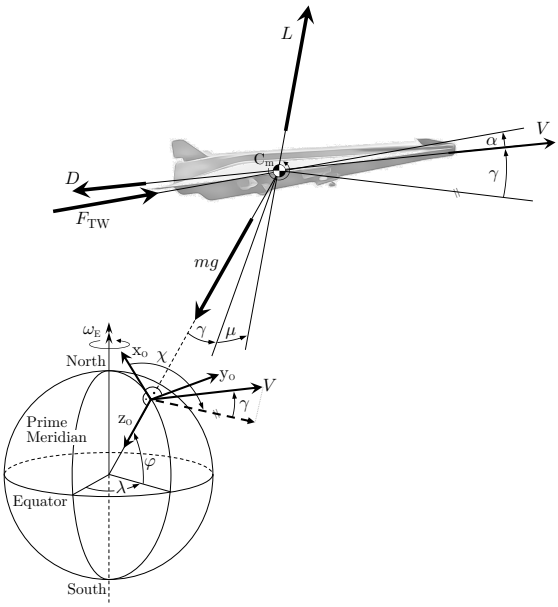

Fig 3. Flight dynamics modelling of the hypersonic aircraft in the absence of atmospheric wind

[5] The HTCM is a derivative of the Trajectory Calculation Module (TCM) software tool [20], which is implemented in MATLAB© and has been developed by DLR Air Transportation Systems since 2009.

Describing the motion of an aircraft using a geodetic system in non-rotating geocentric coordinates (an inertial frame) at the aircraft's *center of gravity* (CoG) allows for the consideration of Earth's rotational speed ω_{E}. The aircraft's CoG position is defined in spherical coordinates with geographical longitude λ, geocentric latitude φ, and distance $r_{\mathrm{E}} + h$ from the center of Earth. Additionally, the kinematic system, also located at the CoG of the moving vehicle, results from rotating the geodetic system with χ (z_{O}-axis) and γ (y_{K}-axis). Another consecutive rotation with μ (x_{K}-axis) yields the intermediate kinematic system. Lastly, tilting this system by the angle of attack α ($y_{\bar{\mathrm{K}}}$-axis) results in the body-fixed frame (see Fig 3).

2.2. External Forces

The external forces acting at the CoG of the hypersonic aircraft are depicted in Fig 3 and are generated by an aerodynamic and an engine model. These models are both fed with processed flight performance data. The aerodynamic model provides the lift and drag force as well as the angle of attack:

$$L = \frac{1}{2} \cdot \rho \cdot V^2 \cdot S \cdot C_L \qquad D = \frac{1}{2} \cdot \rho \cdot V^2 \cdot S \cdot C_D(\mathrm{Ma}, C_L) \qquad \alpha = (\mathrm{Ma}, C_L) \tag{3}$$

Here, S is the wing reference area of the vehicle that is given by 2517 m². Note that due to the absence of atmospheric wind, the fight-path velocity corresponds to the true airspeed of the vehicle. To decrease the computational time needed per simulation step, we only consider small inclination angles and small angles of attack for determining the aerodynamic lift coefficient so that C_L can be formulated as ([21])

$$C_L = C^* \cdot \left\{ mg + 2 \cdot m \cdot \omega_{\mathrm{E}} \cdot V \cdot \sin\chi \cdot \cos\varphi + m \cdot {\omega_{\mathrm{E}}}^2 \cdot \cos^2\varphi \, (r_{\mathrm{E}} + h) - \underbrace{m \cdot V\left[\sin\chi \cdot \dot{\lambda} \cdot \cos\varphi + \cos\chi \cdot \dot{\varphi}\right]}_{\text{Term } \star} \right\}, \tag{4}$$

with $C^* = 2/(\rho \cdot V^2 \cdot S \cdot \cos\mu)$. Since the aerodynamic drag coefficient and the angle of attack depend on the Mach number Ma and lift coefficient, we use stationary trim tables as data input to interpolate for C_D and α, which are shown in Fig 4. This encompasses the contribution of the aerodynamic control surfaces involved in the longitudinal movement such as canards, elevons and bodyflaps (see Fig 1), to bring the pitching moment coefficient C_m to zero ensuring static stability, namely $\delta C_m/\delta\alpha < 0$, at every point of the trajectory. Additional contributions to the built-up approach of the stationary trim tables, as e.g. the non-negligible effect from the misalignment of the thrust vector with the vehicle's x-axis, can be found in [3]. The U.S. Standard Atmosphere 1976 [22] serves as the foundation for modeling the static states of the atmosphere incorporated in Eq. 3 and 4 by establishing the correlation between locally prevailing atmospheric conditions, such as air density ρ, and the geopotential height $H_{\mathrm{G}} = (r_{\mathrm{E}} \cdot h)/(r_{\mathrm{E}} + h)$, based on reference values at mean sea level.

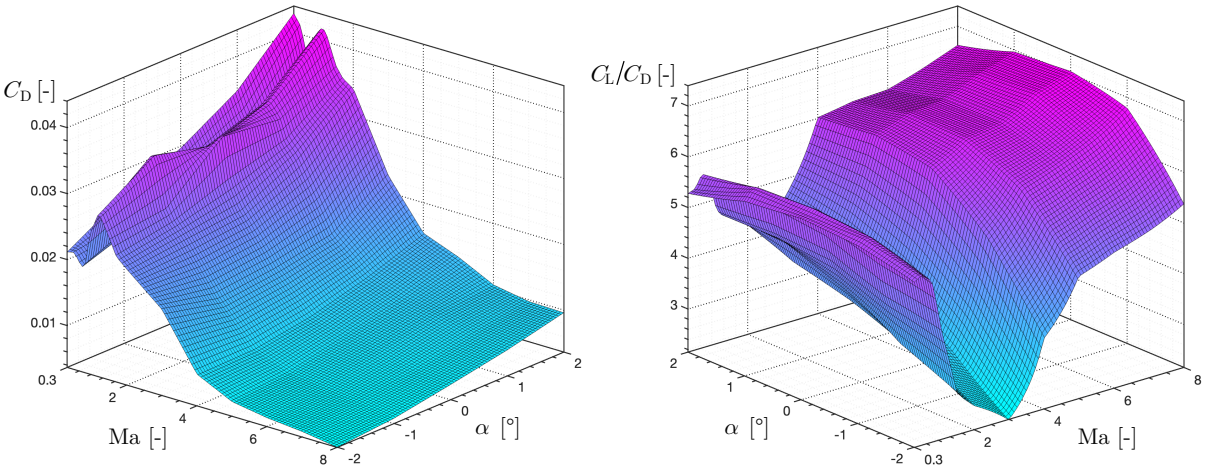

Fig 4. Trim tables used for HTCM simulation of MR3: Drag coefficient $\mathrm{C_D}$ and aerodynamic efficiency ($\mathrm{C_L/C_D}$-ratio) as function of Mach number Ma and angle of attack α (data from [3])

The engine model is tailored to the STRATOFLY-MR3 powerplant, featuring a combined turbojet (ATR)-scramjet (DMR) propulsion system, with each propulsion unit represented by distinct 3D lookup tables. This mathematical model interpolates the net thrust, which inherently incorporates both the gross thrust and the internal drag contribution, as a function of altitude, Mach number and equivalence ratio ϕ_{L}:

$$F_{\mathrm{TW}} = F_{\mathrm{TW,net}}\left(h, \mathrm{Ma}, \phi_{\mathrm{L,TW}}\right) \tag{5}$$

The equivalence ratio for LH_2 in air combustion is defined as the ratio of the actual hydrogen/air mixture ratio to the stoichiometric hydrogen/air ratio and can be interpolated from the ATR/DMR tables for the current engine operating conditions, which are described by the altitude and Mach number:

$$\phi_{\mathrm{L,TW}} = \frac{\left(\frac{\dot{m}_{\mathrm{LH2}}}{\dot{m}_{air}}\right)_{actual}}{\left(\frac{\dot{m}_{\mathrm{LH2}}}{\dot{m}_{air}}\right)_{stoich}} = \frac{\dot{m}_{\mathrm{LH2}} \cdot 34.33}{\dot{m}_{air}} = f(h, \mathrm{Ma}) \tag{6}$$

Another engine characteristic provided by the model is the fuel consumption of the ATR/DMR propulsion unit. This is obtained through linear interpolation from the net lookup tables and scaled linearly using the virtual throttle ratio δ_{TW}, as outlined in Section 2.4:

$$\dot{m}_{\mathrm{TW}} = \dot{m}_{\mathrm{TW,net}}(h, \mathrm{Ma}, \phi_{\mathrm{L}}) \cdot \delta_{\mathrm{TW}} \tag{7}$$

Fig 5 and 6 show the nominal operating limitations of the ATR and DMR propulsion unit for flights with stoichiometric combustion ($\phi_{\mathrm{L,max}} = 1$) and for a flight without LH_2 supply ($\phi_{\mathrm{L,min}} = 0$). In terms of the ATR lookup tables, engine properties are given along discrete interpolation points for a flight envelope of $\mathrm{Ma} \in [0.3, 4]$ and $h \in [0\ \mathrm{km}, 25\ \mathrm{km}]$, whereas the DMR lookup tables provide engine characteristics for Mach numbers ranging from 4 to 8 and altitudes ranging from 24 to 25 km. To further increase the net thrust at critical points along the flight trajectory, an over-stoichiometric combustion of $\phi_{\mathrm{L,max}} = 1.5$ can be realized. The resulting 50% increase in LH_2 net consumption is depicted alongside the net thrust increase in Fig 6 (marked in red); exemplary covering a Mach number range from 4 to 5.

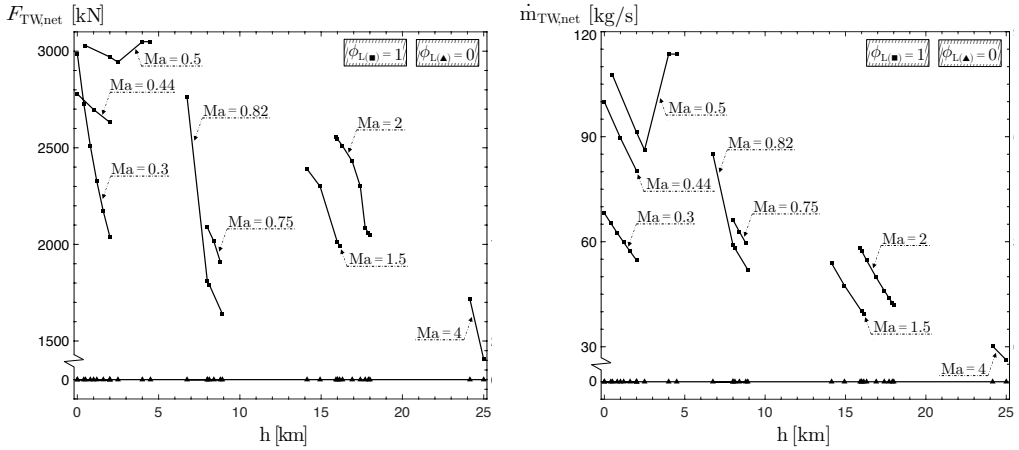

Fig 5. ATR lookup tables used for HTCM simulation of MR3: Total net thrust $\mathrm{F_{TW,net}}$ and total net fuel consumption $\dot{\mathrm{m}}_{\mathrm{TW,net}}$ as function of Mach number Ma and height h (data from [23])

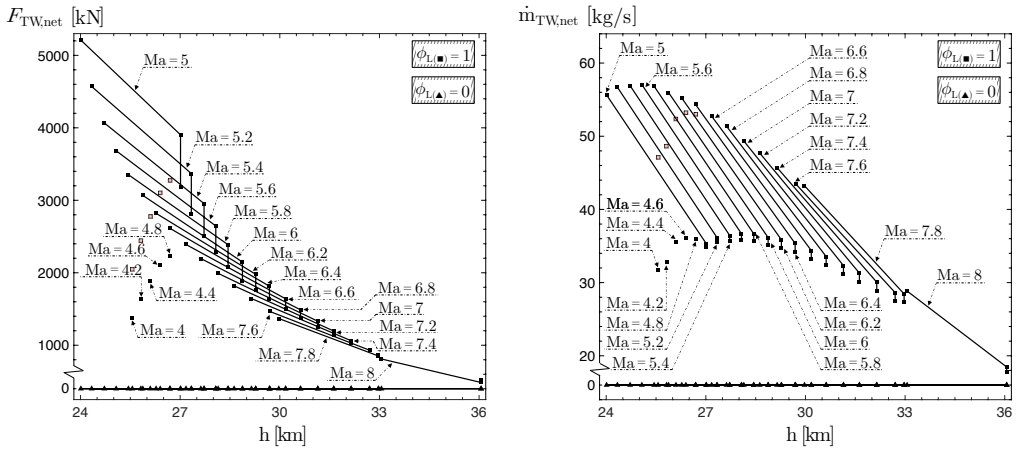

Fig 6. DMR lookup tables used for HTCM simulation of MR3: Total net thrust $\mathrm{F_{TW,net}}$ and total net fuel consumption $\dot{\mathrm{m}}_{\mathrm{TW,net}}$ as function of Mach number Ma and height h (data from [24])

2.3. Load Factors

To uphold the concept of travel comfort while flying with hypersonic speeds, anthropometric passenger g-forces must be guaranteed over the whole flight envelope, which are understood as physical loads on the passengers' musculoskeletal system that have been adapted to tolerable levels of force magnitude. The physical unit of g-forces is meters per second squared ($\mathrm{m/s^2}$), whereas an equivalent dimensionless notation is referred to as load factor. In orthogonal direction to the flight path, the so-called normal load factor can be expressed by the ratio of the lift force L to the weight force mg of the aircraft, corrected by the fictitious force component resulting from the curvature of Earth:

$$n_\mathrm{z} = \frac{L}{mg} - \underbrace{\frac{V^2 \cdot \cos^2\gamma}{g \cdot (r_\mathrm{E} + h)}}_{\text{Term } \bigstar\bigstar} \tag{8}$$

Note that the posterior fictitious term ($\bigstar\bigstar$) is identical to term ($\bigstar$) of Eq. 4. Additionally, at a hypersonic cruise speed of Mach 8 and an altitude of up to $36\ \mathrm{km}$, the normal load factor is calculated to 0.9, which corresponds to an effective (long-term) g-force of $-0.1g$, causing passengers to feel as if they are lifted from their seats ([25]). Flight maneuvers that generate an additional (short-term) g-force perpendicular to the flight path are coordinated (non-slip) turn flights as well as climbing or descending flights. Under these flight conditions, the normal load factor is determined as follows:

$$n_\mathrm{z} = \underbrace{\frac{1}{\cos\mu} - \frac{V^2 \cdot \cos^2\gamma}{g \cdot (r_\mathrm{E} + h)}}_{\text{Turn flight}} = \underbrace{\frac{V \cdot \dot{\gamma}}{g} + \cos\gamma - \frac{V^2 \cdot \cos^2\gamma}{g \cdot (r_\mathrm{E} + h)}}_{\text{Climb/Descend flight}} \tag{9}$$

In direction of the flight path, the axial load factor is specified as the acceleration capacity, derived from the equilibrium between thrust F_TW and drag D force, normalized by the weight force mg and corrected by the weight force's sine component in the tangential plane relative to the flight-path velocity:

$$n_x = \frac{F_\mathrm{TW} - D}{mg} + \sin\gamma \tag{10}$$

During HTCM simulations, the flight control system outlined in Section 2.4 prevents dynamic exceedance of the load factor limits. To maintain passenger comfort over the whole flight envelope, n_z is constrained to a range of $[+0.85g;\ +1.2g]$, while n_x is restricted to a range of $[-0.2g;\ +0.3g]$.

2.4. Closed-Loop Control System for Nonlinear Simulation

For a high-precision path-guidance of the hypersonic aircraft according to position, translation and time the closed-loop flight control system shown in Fig 7 is used within the HTCM software, which comprises of a nonlinear plant model (see Section 2.1), four linear feedback controllers and a pure feed-forward control to affect the aircraft dynamics as well as a state generator to define the reference (commanded) aircraft states or rather the target condition vector $\vec{w} = [V_\mathrm{c},\ \chi_\mathrm{c},\ \gamma_\mathrm{c},\ \mu_\mathrm{c},\ n_\mathrm{x,c}] \in \mathbb{R}^5$ in each flight phase of the mission. This implies that the four controlled aircraft states V, χ, γ and μ are allocated among five pseudo controls $\tilde{\tau}_{\dot{V}}$, $\tilde{\tau}_{\dot{\chi}}$, $\tilde{\tau}_{\dot{\gamma}}$, $\tilde{\tau}_{\dot{\mu}}$ and $F_\mathrm{TW,c}$ to bring the state control error vector $\vec{e} = [\mathrm{e}_V,\ \mathrm{e}_\chi,\ \mathrm{e}_\gamma,\ \mathrm{e}_\mu] \in \mathbb{R}^4$ to zero, utilizing both a proportional-integrating (PI) control algorithm to formalize the control laws and a thrust force mapping to ensure anthropometric passenger g-forces. Additionally, limiters are included into the closed-loop system to ensure that the input vector of the plant $\vec{u} = [\tau_{\dot{V}},\ \tau_{\dot{\chi}},\ \tau_{\dot{\gamma}},\ \tau_{\dot{\mu}},\ F_\mathrm{TW,c}] \in \mathbb{R}^5$ stays bounded at any time of the numerical simulation.

Velocity Controller

To control the speed of the aircraft, the flight-path velocity serves as a model state, which corresponds to the true airspeed (TAS) in a windless, static atmosphere. Depending on the specific flight phase, the guidance command can be either a target calibrated airspeed (CAS) $V_\mathrm{CAS,c}$ or a target Mach number $\mathrm{Ma_c}$, both of which are mathematically converted to the equivalent TAS. Hence, the speed control error is

$$e_V = \left[V - V_\mathrm{TAS,c}(\mathrm{Ma_c}, T)\right] \qquad e_V = \left[V - V_\mathrm{TAS,c}(V_\mathrm{CAS,c}, \rho, p)\right] \tag{11}$$

When formalizing the control law for the velocity controller, the control error is proportionally combined and integrated over time, then negatively amplified by the constant factors k_P and k_I, respectively:

$$\tilde{\tau}_{\dot{V}} = -k_\mathrm{P} \cdot e_V - k_\mathrm{I} \cdot \int (e_V)\, dt \tag{12}$$

As the pseudo-control law has the physical unit of an acceleration, it is limited to $\tilde{\tau}_{\dot{V}} \in [-0.2g; 0.3g]$ per numerical simulation time step.

Flight-Path Controller

To compensate impermissible deviations from a desired climb or descent angle, the vertical navigation guidance command γ_c is subtracted from the state feedback γ to define the control error $e_\gamma = (\gamma - \gamma_c)$. This serves as the basis for contriving the pseudo-control law:

$$\tilde{\tau}_{\dot{\gamma}} = -k_\mathrm{P} \cdot e_\gamma - k_\mathrm{I} \cdot \int (e_\gamma)\, dt \tag{13}$$

Since Eq. 13 has the inherent unit of a rational speed, it is limited to $\tilde{\tau}_{\dot{\gamma}} \in [-0.024°/s; 0.068°/s]$ per each time step of the numerical simulation (refer to Eq. 9).

Navigation Controller

The navigation controller's objective is to control the remaining flight-path angles χ and μ in such a way that the lateral navigation guidance commands, namely a target bank angle μ_c and a target course χ_c, are tracked while maintaining tolerable passenger load factors. The target course is associated with the desired ground track of user waypoints (WPs) $[\lambda_{\mathrm{c},1}|\varphi_{\mathrm{c},1} \ \ldots \ \lambda_{\mathrm{c,n}}|\varphi_{\mathrm{c,n}}] \in \mathbb{R}^{2\times \mathrm{n}}$, whereas the target flight-path bank angle results from the kinematics of stationary (non-slip) turn flights:

$$\mu_\mathrm{c} = \arctan\left(\frac{V^2}{g \cdot r_\mathrm{t}} \cdot \operatorname{sign} \Delta\chi\right) = \arctan\left(\sqrt{n_{\mathrm{z,max}}^2 - 1} \cdot \operatorname{sign} \Delta\chi\right) \tag{14}$$

Here, r_t denotes the turn radius, which is inherently correlated to the maximal normal load factor $n_{\mathrm{z,max}}$, and $\Delta\chi$ is the course deviation between the respective WPs. By defining the control errors $e_\chi = (\chi - \chi_\mathrm{c})$ and $e_\mu = (\mu - \mu_\mathrm{c})$, we can write the pseudo-control laws as

$$\tilde{\tau}_{\dot{\chi}} = -k_\mathrm{P} \cdot e_\chi - k_\mathrm{I} \cdot \int (e_\chi)\, dt \qquad \tilde{\tau}_{\dot{\mu}} = -k_\mathrm{P} \cdot e_\mu - k_\mathrm{I} \cdot \int (e_\mu)\, dt \tag{15}$$

As per [26], civil passenger aircraft require approximately $5\ s$ to reach a target bank angle of $30°$. Thus, $\tilde{\tau}_{\dot{\mu}}$ is preliminary constrained within the acceptable range of $[-6°/s; +6°/s]$. Similarly, for $\tilde{\tau}_{\dot{\chi}}$, the control limitation is directly derived from Eq. 9, resulting in a permissible range of $[-0.16°/s; +0.16°/s]$.

Thrust Force Mapping

Based on Eq. 1 and 10, we model the ATR/DMR thrust force as pure feedforward control devoid of time-varying delays:

$$F_{\mathrm{TW,c}} = \frac{1}{\cos\alpha}\left\{mg \cdot n_{\mathrm{x,c}} + D + {\omega_\mathrm{E}}^2\,(r_\mathrm{E} + h)\,\cos\varphi \cdot [\cos\gamma \cdot \cos\chi \cdot \sin\varphi - \sin\gamma \cdot \cos\varphi]\right\} \tag{16}$$

This scalar mapping guarantees that the maximal $F_{\mathrm{TW,c,max}}$ and minimal $F_{\mathrm{TW,c,min}}$ thrust force commands correspond to the maximal $n_{\mathrm{x,max}}$ and minimal $n_{\mathrm{x,min}}$ load factors based on the guidance command $n_{\mathrm{x,c}}$. The operating condition of the ATR/DMR propulsion unit is ascertained through the virtual throttle ratio, which is calculated as the quotient of the commanded thrust force to the interpolated thrust, given by the engine model, and used for linear scaling of the fuel consumption calculation, as indicated in Eq. 7:

$$\delta_\mathrm{TW} = \frac{F_{\mathrm{TW,c}}}{F_\mathrm{TW}} \tag{17}$$

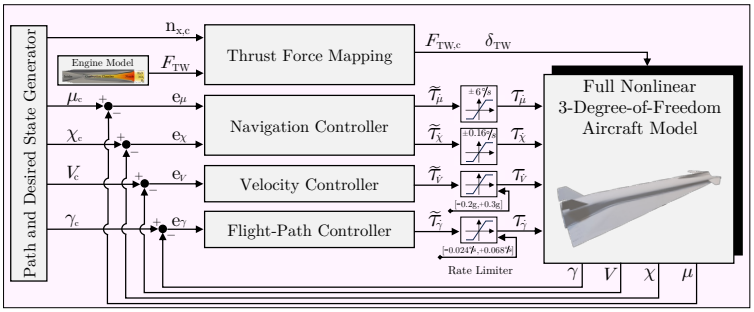

Fig 7. Flight-path control system for feedback-based guidance of hypersonic aircraft

2.5. Emission Model

Given the significant impact of pollutant quantity and species on climate responses in terms of changes in the chemical composition of the atmosphere, the task of the emission model is to meticulously expand the engine reactions delineated in Section 2.2 to encompass the gaseous engine emissions of NO, H_2O, and H_2 generated during hypersonic flight. For this purpose, the model extends the HTCM state variables by the emission mass flows $\dot{m}_i$ as well as the emission quantities m_i of the individual trace substances with $i \in \{\mathrm{NO}, \mathrm{H_2O}, \mathrm{H_2}\}$. To determine the emission properties of the ATR/DMR propulsion unit, 3D lookup tables are included into the model. These tables specify the emission indices EI_i of the trace species as a function of h, Ma and ϕ_L, indicating the quantity of the exhaust gas product g_i generated per kilogram of fuel burned (kg_{LH2}). By evaluating these tables (refer to Fig 8 and 9)[6] via a linear interpolation routine for each time step t of the 4D-trajectory, the emission mass flows can be calculated using Eq. 7:

$$\dot{m}_i(t) = \mathrm{EI}_i(h, \mathrm{Ma}, \phi_\mathrm{L}) \cdot \dot{m}_\mathrm{TW} \tag{18}$$

The partial quantities of NO, H_2O, and H_2 emissions released along the flight path are calculated through the multiplication of Eq. 18 with the numerical integration step size Δt, resulting in 3D emission profiles:

$$m_i(t) = \dot{m}_i(t) \cdot \Delta t \tag{19}$$

To determine the total emission quantities of the hypersonic flight mission, the time integral is calculated over the emission mass flows from the start (t_0) to the end time (t_f) of the numerical simulation:

$$m_i = \int_{t_0}^{t_f} \dot{m}_i(t)\, dt \tag{20}$$

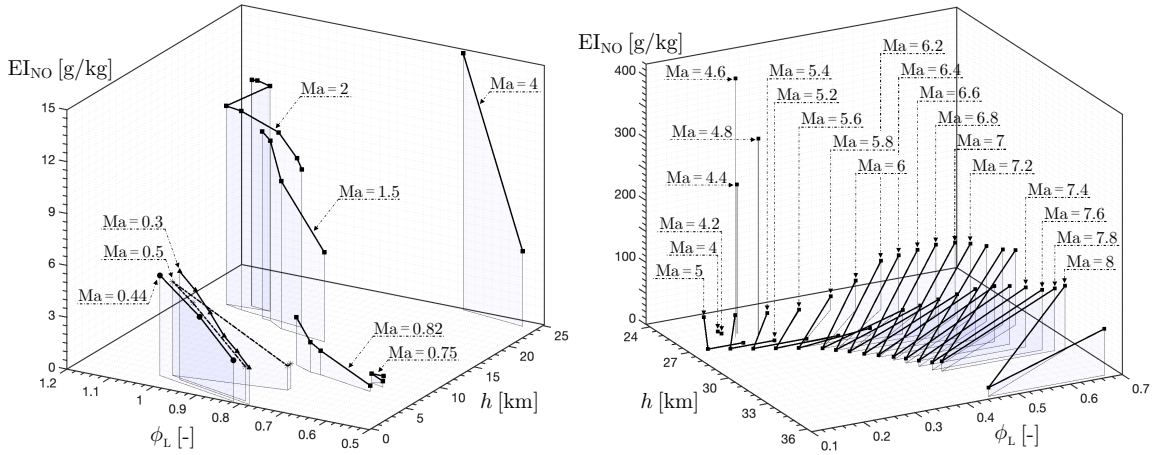

Fig 8. $\mathrm{EI_{NO}}$ as function of Ma, h and ϕ_L (data from [27] scaled with 0.147 according to [28])

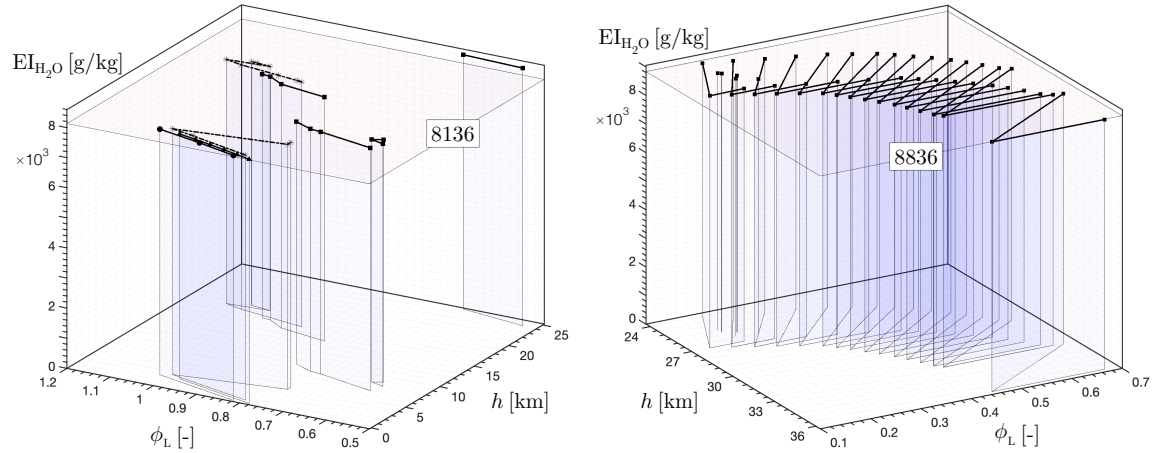

Fig 9. $\mathrm{EI_{H2O}}$ as function of Ma, h and ϕ_L including $\varnothing\mathrm{EI_{H2O}}$ for ATR/DMR mode (data from [27])

[6] $\mathrm{EI_{H2}}$ is ranging from 12.29 g/kg to 192.24 g/kg in ATR and from 0.00022 g/kg to 1.16 g/kg in DMR mode ([27]).

3. Sonic Boom Carpet Computation

When an object moves through the atmosphere at speeds faster than the speed of sound, it unavoidably emits compression waves that are sensual perceived as loud bangs by an observer on the ground. The wave propagation effect of these shock waves can usually be modelled with locally planar wave models, when the radial distance from the source is sufficiently large. This assumption can be summarized with the term *far-field*, in contrast to the *nearfield*. In other words, the far-field can be considered as the area of the sound field, in which the curvature of the wave front is negligible for small elements of the wave front, due to its large distance from the source. Under this assumption, planar wave propagation models can be employed to describe the motion characteristics of small pieces of the shock wave front.
With the far-field assumption, the aircraft is considered as a moving point mass source, which generates a conical shock wave front, i.e., the Mach cone. Due to the locally planer wave assumptions in the far-field, ray theory can be used to describe the propagation of the shock wave front. This theory is based on geometric acoustics to estimate the shock wave front behaviour in an inhomogeneous medium, such as the atmosphere of Earth ([29]).

3.1. Ray Tracing Algorithm

We ascertain the geographic positions of the sonic boom shock waves on ground by applying ray theory equations within a ray-tracing algorithm that was previously described in [14]. This algorithm primarily relies on coupled differential equations in a tensor formulation, which are solved numerically to compute the ray paths ([30]):

$$\frac{d\vec{r}}{dt} = a \cdot \vec{n} + \vec{w} \qquad \frac{d\vec{n}}{dt} = (\boldsymbol{I} - \vec{n} \otimes \vec{n}^T)\nabla(a + \vec{w} \circ \vec{n}) \tag{21}$$

Here, $\vec{n} \in \mathbb{R}^3$ denotes the wave front normal vector, which is the vector perpendicular to the shock wave front surface, $\vec{r} = [x \quad y \quad z]^{\mathrm{T}}_{\mathrm{N}} \in \mathbb{R}^3$ represents the position vector of that specific shock wave front in the navigation frame, $\vec{w} \in \mathbb{R}^3$ denotes the wind speed vector, t denotes the time variable of the numerical simulation, $\boldsymbol{I}$ symbolizes the unit tensor and a is the ambient speed of sound that is given by the ideal gas law:

$$a = \sqrt{\kappa \cdot R \cdot T} \tag{22}$$

In Eq. 22, κ denotes the adiabatic index of air, set to a value of 1.4, while R represents the specific gas constant of air, with an empirical value of $287.058\,\mathrm{J/kg\,K}$. The ambient temperature is described by T. To initiate the tracing procedure, we define the initial position of a specific ray by extracting the position states λ, φ and h of the aircraft state vector $\vec{x}$ for a valid flight condition ($\mathrm{Ma} > 1$). The initial orientation of the ray is likewise defined by using the orientation states χ, γ and μ of the aircraft. This also includes the initialization of the Mach angle $\sigma = \sin^{-1}(1/\mathrm{Ma})$, since the rays start their propagation perpendicular to the Mach cone. The only varying parameter that distinguishes rays which are sent out perpendicularly to the Mach cone surface is the azimuthal angle ϑ. Note that this is a peculiarity of the sound field of a supersonically moving source, as the wave front is not propagating in a spherical manner. Fig 10 shows the concept of the ray tracing approach.

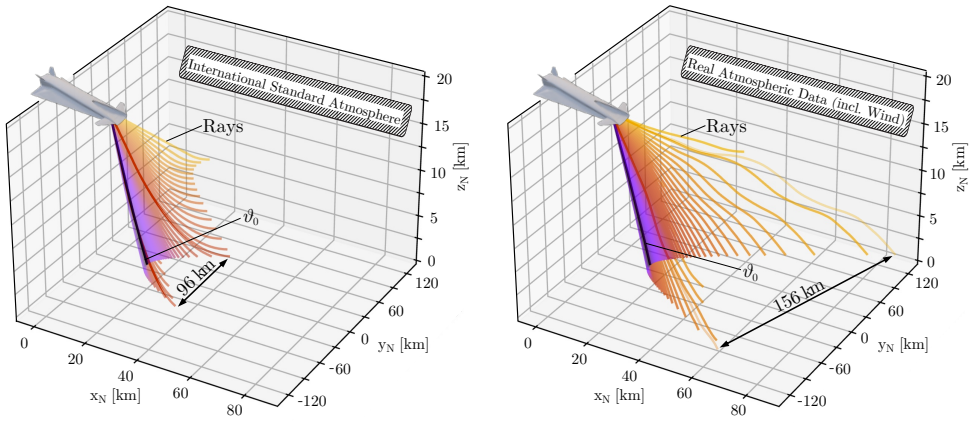

Fig 10. Schematic view of tracing a sonic boom shock wave front in the supersonic flight regime for different atmospheric conditions (left: ISA; right: Real atmospheric data incl. wind)

The rays start perpendicular to the Mach cone surface (not depicted), such that they propagate towards the front of the aircraft's initial position. Depending on the azimuth angle, the propagation begins downwards (i.e., on-track ray at $\vartheta_0 = 0°$; highlighted in black) or with a lateral deviation (i.e., off-track rays with $\vartheta \neq 0°$; lighter colours depict a higher deviation in relation to ϑ_0). As the aircraft travels faster than the shock wave front, it should be mentioned, that the rays depicted in Fig 10 represent the progression of small parts of the shock wave front at every time step $t_0 + \Delta t$ of the numerical simulation until they reach the ground (or bend upwards), while the aircraft is only depicted at its initial position for t_0. Due to refraction in the atmosphere (as the temperature increases towards the ground), the sonic rays tend to bend up before reaching the ground. All remaining rays that still reach the ground, define the primary sonic boom carpet, as this is the region, where the sonic boom shock wave front emitted at that specific location will hit the ground. The impact points of the lateral cut-off rays define the carpet width, which can be scaled up notably when comparing the tracing results for a windless standard atmosphere (ISA, left) [22] and a realistic atmosphere (right), derived from measured weather data including wind.

4. Trajectory Optimization

As 4D solution of the numerical simulation, the flight trajectory maps the flight profile (3D) of the aircraft as a function of flight time (1D). This profile can be enhanced using both vertical (1D) and lateral (2D) optimization algorithms, which are presented below. They yield an emission- and noise-optimal 3D flight profile based on operational changes in cruise altitude (1D) and flight path waypoints (2D).

4.1. Vertical Optimization (1D)

The vertical trajectory optimization entails a numerical search algorithm designed to assess the potential for mitigating the overall emissions of NO and H_2O in comparison to a reference trajectory. The relative potentials are called $EQMP_{NO}$, respectively $EQMP_{H2O}$. The algorithm relies on a brute force method, which allows the HTCM to be triggered with varying operational measures that define the trajectory simulation such as the target initial cruise altitude (ICA; user input[7]). To activate the iterative calculation process shown in Fig 11, the algorithm incrementally adjusts the ICA for each HTCM simulation in small constant steps $\Delta\mathrm{ICA}$ until the search interval is completed. The total number of calculation steps n_{ICA} is referring to the search limits $[\mathrm{ICA}_{\mathrm{min}}, \mathrm{ICA}_{\mathrm{max}}]$ and can be determined as follows:

$$n_{\mathrm{ICA}} = \frac{\mathrm{ICA}_{\mathrm{max}} - \mathrm{ICA}_{\mathrm{min}}}{\Delta\mathrm{ICA}} + 1 \tag{23}$$

The attainable set of mitigation potentials is computed by assessing each solution of the iteration based on Eq. (20) and comparing it as relative ratio to the reference solution (indexed as 'ref'):

$$\mathrm{EQMP}_{\mathrm{NO,j}} = 100 \cdot \frac{m_{\mathrm{NO,j}}(\mathrm{ICA_j})}{m_{\mathrm{NO,ref}}} - 100 \qquad \mathrm{EQMP}_{\mathrm{H2O,j}} = 100 \cdot \frac{m_{\mathrm{H2O,j}}(\mathrm{ICA_j})}{m_{\mathrm{H2O,ref}}} - 100 \tag{24}$$

with $j \in \{1, 2 \ \ldots \ n_{\mathrm{ICA}}\}$. Finally, the minima $\mathrm{EQMP}^*_{\mathrm{NO}}$ and $\mathrm{EQMP}^*_{\mathrm{H2O}}$ are determined from Eq. (24), which are referred to those trajectories that have the highest potential for reducing the environmental impacts in terms of total emissions. Note that the corresponding optimal ICA^* may differ for these minima.

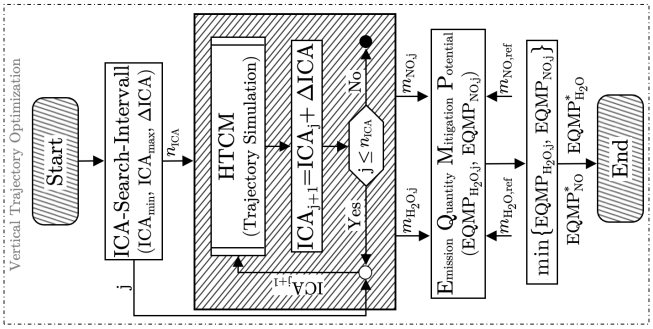

Fig 11. Schematic illustration of numerical search algorithm for EQMP approach

[7] The HTCM user inputs are as follows: 1) Numerical integration step size Δt 2) Cruise Mach number Ma, 3) Cruise altitude ICA 4) Route waypoints $[\lambda_1|\varphi_1 \ \ldots \ \lambda_{\mathrm{n}}|\varphi_{\mathrm{n}}]$ 5) Take-off mass m_0 6) Continuous Climb Cruise (CCC; yes|no)

4.2. Lateral Optimization (2D)

The lateral trajectory optimization relates to the sonic boom carpet propagation and involves an iterative route design process, as illustrated in Fig 12, to automatically modify the ground track of the trajectory based on encountered infringements of the boom carpet. These infringements occur when sonic booms (SBs) reach the ground or inhabited areas along the flight path, leading to routes that are predominantly over water. Similar to the vertical optimization, the algorithm allows the HTCM to be called with varying operational measures that predefine the trajectory simulation such as the route WPs $[\lambda_1|\varphi_1 \ \dots \ \lambda_\mathrm{n}|\varphi_\mathrm{n}]$. Within each iteration step, these waypoints are modified until the 4D-trajectory becomes noise-optimal, supposing that constraint (ii-1) is satisfied. The process comprises the following steps or software tools, whereby their content-related algorithmic functionality is reproduced below in simplified form to support a compact formulation:

A) Initial Waypoints
The initial flight route for a hypersonic mission is drafted in Google Earth[8] for a given city pair connection, or so-called *Stratoports* [9]. This initial draft incorporates a preliminary approximation of the sonic boom carpet, ensuring sufficient buffer zones on both sides of the flight path relative to the coastlines. Next, an initial set of route waypoints, exclusively positioned over water, can be manually derived and utilized as input for the trajectory simulation in step B.

B) Hypersonic Trajectory Calculation Module (HTCM)
The HTCM software tool (refer to Section 2) serves as the mission simulator, employed to compute the 4D-trajectory based on predefined user inputs, which also include the initial set of route WPs derived in step A. As input for the sonic boom carpet computation the time-history of the aircraft state vector $\vec{x}(t)$ is transferred to step C.

C) Sonic Boom Carpet
The sonic boom ray tracing algorithm (refer to Section 3) is used to calculate the sonic boom carpet for the hypersonic flight mission based on $\vec{x}(t)$ as input. The output of C encompasses the position vector $\vec{r}_\mathrm{SB} = [\lambda_{\mathrm{SB}-1}|\varphi_{\mathrm{SB}-1} \ \dots \ \lambda_{\mathrm{SB}-\mathrm{n}}|\varphi_{\mathrm{SB}-\mathrm{n}}]^\mathrm{T} \in \mathbb{R}^{\mathrm{n}\times 2}$ of all (n) sonic rays reaching the ground. These shock wave coordinate pairs define the outermost boundary of the geometric sonic boom carpet as polygonal chain.

D) Check Sonic Boom Infringements (Constraint ii-1)
To ensure compliance with operational constraint (ii-1), we employ the land_or_ocean.m [31] MATLAB function during step D, which relies on a polygonal approximation to delineate land masses and oceans as mathematical meshes. This function takes $\vec{r}_\mathrm{SB}$ as input vector and returns a vector of binary classifiers indicating whether the sonic shock wave coordinate pairs are located on land or water.

E) Flight-Path Modification Module (FPMM)
The Flight-Path Modification Module (FPMM) is a software tool developed to modify the initial flight path of a reference trajectory using a geometric approach aimed at minimizing the impact of noise emissions from primary sonic booms on inhabitant areas. For the sake of consistency, this approach relies on great circle formulas for determining distances and course angles between trajectory-, route- and SB-related geodetic model states. Thus, tool inputs are not only provided from step D, but also from B and C. With regard to the binary classifiers from step D, land-based SB coordinate pairs are clustered and averaged arithmetically (indexed as 'SB,land,i') to obtain the shortest distance to the geodetic trajectory states:

$$d_\mathrm{min} = \min\left[\vec{r}_\mathrm{E} \cdot \underbrace{\cos^{-1}\left\{\sin\bar{\varphi}_\mathrm{SB,land,i} \cdot \sin\vec{\varphi}(t) + \cos\bar{\varphi}_\mathrm{SB,land,i} \cdot \cos\vec{\varphi}(t) \cdot \cos\left(\bar{\lambda}_\mathrm{SB,land,i} - \vec{\lambda}(t)\right)\right\}}_{\sigma}\right] \tag{25}$$

The corresponding magnetic heading (QDM) from the identified trajectory state (indexed as 'min') to the previously defined SB-related model state is calculated as follows:

$$\mathrm{QDM} = \cos^{-1}\left(\frac{\sin\bar{\varphi}_\mathrm{SB,land,i} - \cos\sigma \cdot \sin\varphi_\mathrm{min}}{\sin\sigma \cdot \cos\varphi_\mathrm{min}}\right) \tag{26}$$

[8] Available at www.google.com/earth.

If the distance from the identified trajectory state $\lambda_{\min}|\varphi_{\min}$ to the subsequent or previous route WP is greater than a predefined threshold s_{req}, a new route WP is set. Otherwise, the route WP is adjusted by a user-specified offset $s_{\text{des}} = \sigma_{\text{mod}} \cdot r_{\text{E}}$ so that the modified route WP coordinate pairs (indexed as 'mod') are calculated and incorporated as

$$\varphi_{\text{mod}} = \sin^{-1}\{\sin\varphi_{\min} \cdot \cos\sigma_{\text{mod}} + \cos\varphi_{\min} \cdot \sin\sigma_{\text{mod}} \cdot \cos(\text{QDM} + 180°)\} \tag{27}$$

and

$$\lambda_{\text{mod}} = \lambda_{\min} - \tan 2^{-1}\left(\frac{\sin(\text{QDM} + 180°) \cdot \sin\sigma \cdot \cos\varphi_{\min}}{\cos\sigma_{\text{mod}} - \sin\varphi_{\min} \cdot \sin\varphi_{\text{mod}}}\right) \tag{28}$$

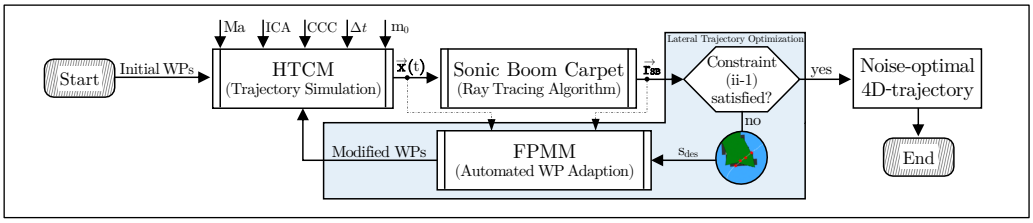

Fig 12. Iterative procedure of lateral trajectory optimization (based on [14])

5. Evaluation of Methodology

The results outlined in this section are based on applying the methodology shown in Section 1.2 on the STRATOFLY-MR3 vehicle, aiming to identify NO- and H_2O-optimal 4D-trajectories as well as their relative emission quantity mitigation potentials ($\text{EQMP}^*_{\text{NO}}$ and $\text{EQMP}^*_{\text{H2O}}$), along with the associated optimal ICA^*_{NO} and $\text{ICA}^*_{\text{H2O}}$ values. By adapting the route waypoints and varying the initial cruise altitude from 30 km to 36 km at a mission level, with a reference flight altitude set at 32 km, operational measures are applied to achieve objective (i) while simultaneously ensuring compliance with operational constraint (ii-1) and (ii-2). The resulting optimized emission profiles are then scaled to represent a world fleet of MR3 aircraft and transformed into a discrete 3D coordinate grid, forming the scientific contribution of the simulation chain for outsourced studies with 3D climate models.

5.1. Setup of Holistic Simulation Chain

The setup of the simulation chain comprises multi-disciplinary inputs, which are partly given in Table 1. The route operated in the year 2075 by MR3 is derived from a database [9] providing initial hypersonic route WPs between distributed city pair connections. As a case study, we evaluate the reference mission from Brussels (BRU) to Sydney (MYA) with a corresponding passenger load factor of 1 - without any fuel planning or reserves. The initial flight conditions remain consistent across all calculated trajectories. We consider a departure from Brussels airport (BRU: $\lambda_0 = 4.49\,|\,\varphi_0 = 50.9$) at an altitude of $h_0 = 45.41$ m, a lift-off velocity of $V_0 = 110$ m/s, and an initial flight-path angle χ_0 of $342.7°$. The flight-path inclination γ_0 and bank angle μ_0 are both initially set to zero, like the initialization of all other HTCM model states.

Table 1. Inputs for holistic simulation chain (refer to Fig 2)

Input	Description	Value	Unit
Ma	Cruise Mach number	8	[-]
ICA_{ref}	Initial cruise altitude (ref)	32 000	[m]
Δt	Integration step size	1	[s]
m_0	Initial Take-Off Weight	410 446	[kg]
ΔICA	Height increment for EQMP	152.4	[m]
r_{E}	Nominal Earth radius	6 356 766	[m]
ω_{E}	Earth rotational speed	$7.292115 \cdot 10^{-5}$	[rad/s]
g_0	Acceleration of gravity at MSL	9.80665	[m/s²]
s_{des}	Great circle offset for FPMM	25 000	[m]

5.2. Optimized Flight Route for Operational Constraint (ii-1) and (ii-2)

Fig 13 shows the optimization results of the iterative route design process aimed at generating a noise-optimal flight path for the reference trajectory, with $\mathrm{ICA_{ref}}$ set at 32 km, satisfying operational constraint (ii-1). The resulting sonic boom carpet edges are depicted in white for exemplary flight segments across the optimized flight path, which is highlighted in yellow in Google Earth[9]. Due to the embedment of the HTCM (see Section 4.2; step B) into the iterative route design process, the navigation controller ensures the adherence of acceptable passenger loads at hypersonic speeds, particularly during turn flights. This further compliance with operational constraint (ii-2) is also evident in Fig 13, with the normal load factor highlighted in orange (left y-axis[10]) across the relative flight time $\mathrm{t/t_f} \in [0,\ 1]$.
We calculated the sonic boom carpet by repeating the tracing approach for every valid flight condition of the 4D-trajectory and connecting the outermost impact points. For the numerical propagation of the rays an open access set of globally discretised weather data was included into the tracing algorithm and interpolated in such a manner that the 3D atmospheric derivatives of temperature and wind speeds are continuous for a variety of exemplary days in the year 2015. This weather dataset was published by the European Centre for Medium-Range Weather Forecasts (ECMWF)[11] and describes the atmospheric state at a specific point in time with a grid resolution of 0.75° × 0.75° (latitude × longitude). The third spatial dimension nodes are discretized in a range from 0 to 40 km, whereby the resolution decreases at higher altitudes. Georeferencing was accomplished using the World Geodetic System 1984 (WGS84) ellipsoid, with each day partitioned into four timesteps to capture the full diurnal cycle. For the carpet simulation, we used a variation of datasets from 2015, as e.g., a 3D grid from November 5th at 06:00 AM.
Note that the iterative route design process failed to converge for the flight segment over Bering Strait, as shown on the right side of Fig 13, primarily due to the considerable width of the boom carpet at this location, ranging from 140 km to 255 km. Given the prior discussions of this issue in [9] and the sparse population in this region, the authors decided to manually adjust the route WPs for that particular flight segment to minimize the observed sonic boom carpet infringements to the greatest extent possible.

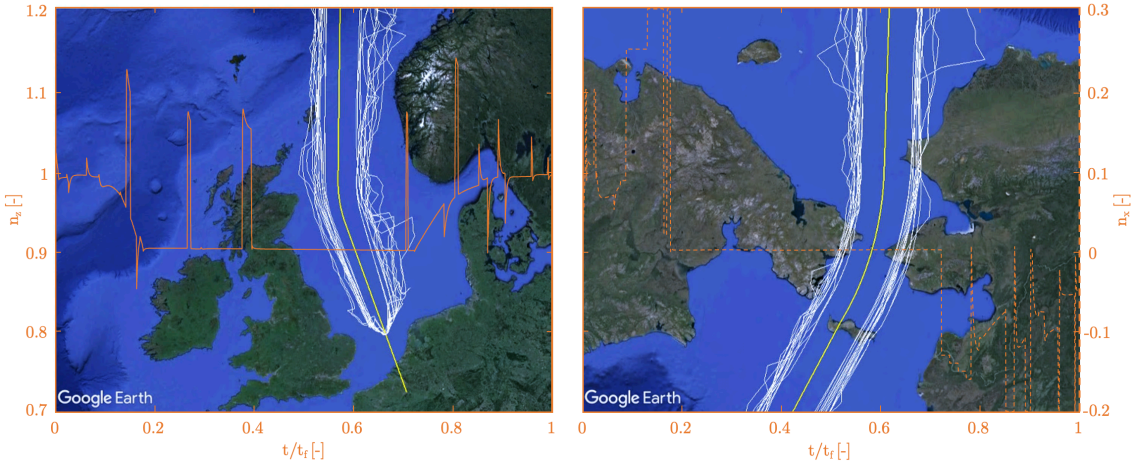

Fig 13. Sonic boom carpet edges (white) and ground track of trajectory (yellow) are illustrated in Google Earth without explicit axis labels (left: North Sea; right: Bering Strait). Additionally, the load factors n_z (left) and n_x (right) are depicted in orange over the relative flight time t/t_f

5.3. Emission Quantity Mitigation Potential (Mission Level)

Fig 14 illustrates the optimization results to quantify the potentials for reducing high-altitude emissions, where each marker represents a 4D-trajectory for different values of the initial cruise altitude. The total quantities of NO emissions m_{NO} (left) and H_2O emissions m_{H2O} (right) are shown each on the left y-axis and the corresponding relative mitigation potentials $\mathrm{EQMP_{NO}}$ and $\mathrm{EQMP_{H2O}}$, which refer to the reference trajectory at $\mathrm{ICA_{ref}} = 32\ \mathrm{km}$, are shown on the right y-axis. By including the residual propellant mass as metric in our analysis, we note that $m_{\mathrm{LH2,f}}$ (top) is insufficient to cover the entire ICA range for the BRU-MYA flight mission. As the aerodynamic drag force decreases with altitude, we observe that the mission is only feasible for ICAs ranging from 31.4 km to 36 km, precluding any additional fuel reserves.

[9] Available at www.google.com/earth.
[10] For the sake of consistency, the axial load factor is also shown on the right y-axis of Fig 13.
[11] 2015 ERA-Interim data, provided by European Centre for Medium-Range Weather Forecasts (www.ecmwf.int).

The comparison between both optimization results reveals that NO emissions notably diminish with altitude, while H_2O emissions remain relatively constant. Consequently, the relative mitigation potential of NO emissions shows a higher variability of up to 19.29 % within the achievable ICA range compared to the H_2O emissions, which only fluctuate by 1.29 %. We find that the NO-optimal solution is located at an altitude of $\mathrm{ICA}^*_{\mathrm{NO}} = 34.75\ \mathrm{km}$ with a $\mathrm{EQMP}^*_{\mathrm{NO}}$ of -18.75 %, which corresponds to a minimal emission quantity of $m^*_{\mathrm{NO}} = 7.7675\ \mathrm{Mg}$. The H_2O-optimal solution is located at an altitude of $\mathrm{ICA}^*_{\mathrm{H2O}} = 32.77\ \mathrm{km}$ with a $\mathrm{EQMP}^*_{\mathrm{H2O}}$ of -0.11 % corresponding to a minimal emission quantity of $m^*_{\mathrm{H2O}} = 1\,519.4\ \mathrm{Mg}$. As H_2O emissions are proportional to the engine's LH_2-flow, the H_2O-optimal trajectory coincides with the fuel-optimal trajectory and yields the highest mission-specific residual propellant mass of $m_{\mathrm{LH2,f}} = 2.271\ \mathrm{Mg}$.

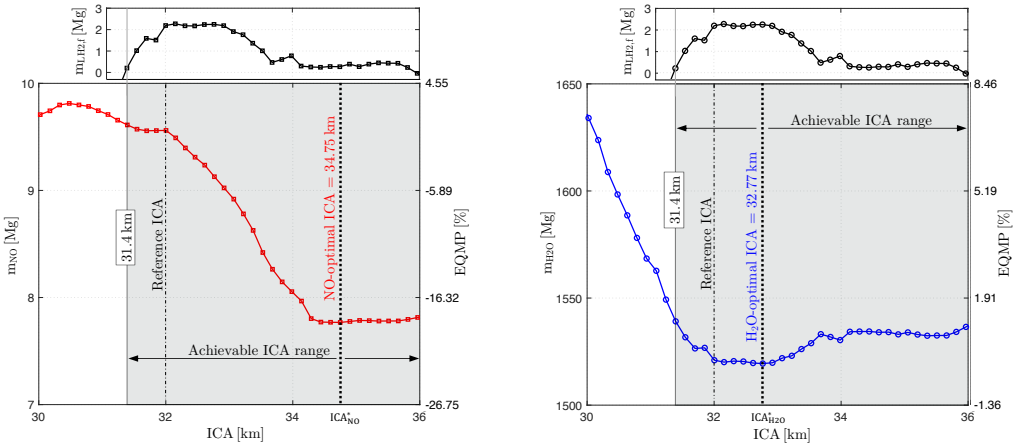

Fig 14. Trajectory Optimization Results (vertical via NO and H_2O) for reference mission; Total emission quantities and relative EQMP over ICA, along with residual quantity of fuel (LH_2)

Fig 15 depicts the resulting 4D-optimal trajectories with respect to NO (left) and H_2O (right) emissions. Both altitude and Mach profiles are plotted over the relative flight time $\mathrm{t/t_f} \in [0,\ 1]$ including the varying magnitude of emission releases denoted by color. This magnitude is defined as the ratio of local emission quantity to the maximum emission quantity within the flight envelope. The vertical flight profile is based on typical flight phases in the subsonic regime and complies with today's regulations of air traffic control (ATC) regarding speed and altitude constraints, such as maintaining a speed limit of 250 kts below FL100 (10 000 ft). As the distance from Brussels to the coast is short, there are no Mach number limitations to prevent sonic booms over land, allowing for an accelerated supersonic climb until reaching the desired ICA. The cruise phase is modelled as a continuous climb cruise (CCC) ensuring a constant Mach number and lift coefficient during cruise, which is assumed to be suitable for HST to approximate real subsonic flights with ATC-required step climbs. The descent to Sydney airport (MYA: $\lambda_{\mathrm{f}} = 150.15\ |\ \varphi_{\mathrm{f}} = -35.89$), reaching a final altitude of $h_{\mathrm{f}} = 5\ \mathrm{m}$ with a final approach speed of $\mathrm{Ma} = 0.325$, includes two level deceleration segments in the hypersonic and supersonic flight regime to ensure stable trim conditions before transitioning into the subsonic regime, where ATC restrictions are met again.

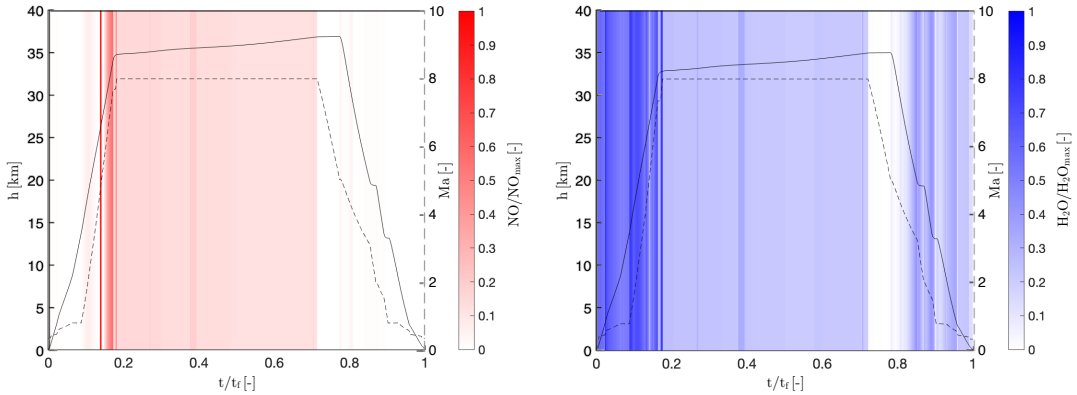

Fig 15. Altitude and Mach profile of the identified NO- and H_2O-optimal trajectories are illustrated across the relative flight time t/t_f, along with colored magnitude of emission release

5.4. Emission Inventories (Fleet Level)

We compute 3D emission inventories for the Brussels to Sydney mission based on a global fleet of MR3 aircraft operated in the year 2075 on the NO-optimal and H_2O-optimal mission profiles (refer to Fig 15) by utilizing DLR's software GRIDLAB [20]. In GRIDLAB, the total quantity of emitted emissions is gridded along the aircraft's flight trajectory using numerical grids with a horizontal resolution of 1° in longitude and latitude and a vertical resolution of 305 m. For simplification, we assume an entry into service (EIS) of MR3 in 2050 and use a generic factor S published by [32] to scale the optimized emission profiles to an annual basis in 2075:

$$S = \underbrace{4}_{\text{New MR3 per Year}} \times \underbrace{25}_{\text{Projeced Years}} \times \underbrace{1}_{\text{Frequency}} \times \underbrace{360}_{\text{Annual Basis}} = 72\,000 \tag{29}$$

Fig 16 shows the longitudinal and latitudinal distribution of the optimized NO (left) and H_2O (right) fleet emissions being aggregated over altitude and normalized per grid cell area. We note that the MR3 fleet emits 0.55926 Tg of NO emissions and 109.398 Tg of H_2O emissions, covering a total travelled distance over ground of 1.3697 Tm.

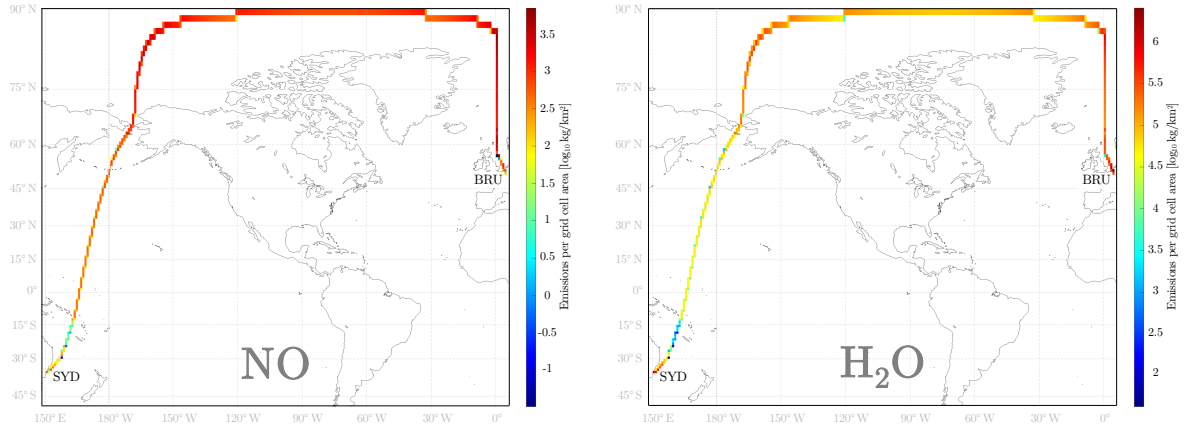

Fig 16. Geographical distribution of emissions (left: NO; right: H_2O) for reference flight mission, vertically aggregated and normalized per grid cell area given in $\log_{10}$ kg/km^2

6. Summary and Future Work

This paper describes a comprehensive methodology to quantify the mitigation potential of NO_x and H_2O emissions for a Mach 8 passenger aircraft fuelled with liquid hydrogen. Realistic operational constraints arising from the current regulatory framework for civil HST operations due to the issue of sonic booms making landfall as well as passenger comfort when flying at hypersonic speeds are addressed in detail in this study. The investigated measures comprise operational changes in the initial cruise altitude and the lateral routing through an adaption of route waypoints. For a reference mission from Brussels (BRU) to Sydney (MYA) our analysis shows that increasing the ICA towards higher altitudes results in a reduced total discharge of both NO_x and H_2O emissions along the aircraft's flight trajectory. We observe that the NO-optimal ICA is located at 34.75 km with a relative mitigation potential of -18.75%, whereas the H_2O-optimal ICA is located at 32.77 km with a relative mitigation potential of -0.11%, both in comparison to the reference ICA being set at 32 km. Additionally, both relative mitigation potentials can be augmented up to -19.18% (NO) and -1.23% (H_2O) by adjusting the reference ICA to 31.4 km, which corresponds to the lower boundary of the mission-specific achievable ICA range. Certainly, these findings provide a new foundation for the redesign of future civil hypersonic passenger aircraft with LH_2-powered scramjet combustors for operating points guaranteeing reduced emission quantities; even though their EIS is not anticipated in the near term.

Based on market forecast data, we scaled the NO- and H_2O-optimal 4D-trajectories by a generic factor from the mission to a full fleet level, established in the projection year 2075. This enabled us to calculate 3D emission inventories with 0.55926 Tg of nitrogen oxides and 109.398 Tg of water vapour emitted by the MR3 fleet per year on the Brussels to Sydney mission.

Future work is planned to calculate 3D emission inventories as well as the emission quantity mitigation potentials for the hypersonic airline network outlined in [9], which is based on assumptions for a realistic

market penetration of civil HST in the future. To be able to evaluate the climate impact from hypersonic aviation, climate response models must be incorporated into ILT's multi-disciplinary simulation chain to calculate adequate climate metrics, such as the radiative forcing (RF). This will not only provide a valid foundation for conducting trade-off analyses between emission- and climate-optimal flight trajectories, but will also facilitate a detailed investigation of the following scientific research questions:

- ☞ How big is the climate impact mitigation potential (CIMP) compared to the EQMP of future HST for the reference mission from Brussels to Sydney?
- ☞ Will the climate-optimal ICA be higher or lower than the emission-optimal ICAs?
- ☞ To what extent the analysed measures can be used to optimize 4D-trajectories of future HST regarding climate impact on a mission level while guaranteeing operational constraint (ii-1) and (ii-2)?
- ☞ What is the CIMP on a fleet level when using the 3D emission inventories of the hypersonic airline network [9] as input?

Acknowledgements

The STRATOFLY project and the MORE&LESS project have received fundings from the European Union's Horizon 2020 research and innovation program under Grant Agreement No. 769246 and 101006856, respectively.

Data Availability

The 3D emission inventories of the MR3 fleet operating along the Brussels to Sydney route on the H_2O- and NO-optimal mission profile in the year 2075, are accessible as NetCDF files at www.zenodo.org with the DOI: http://doi.org/10.5281/zenodo.10818082

References

[1] Anderson, J., Passman, R.: *X-15 The World's Fastest Rocket Plane and the Pilots Who Ushered in the Space Age*. Zenith Press (2014)

[2] Petersen, R. H., Waters, M. H.: Hypersonic transports - Economics and environmental effects. *Journal of Aircraft,* **10**(6):334–341 (1973). https://doi.org/10.2514/3.44372

[3] McClinton, C., Hunt, J., Ricketts, R., Reukauf, P., Peddie, C.: Airbreathing hypersonic technology vision vehicles and development dreams. In: 9th International Space Planes and Hypersonic Systems and Technologies Conference, pp. 1–16. Norfolk, Virginia, USA (1999). https://doi.org/10.2514/6.1999-4978

[4] McClinton, C.: X-43–Scramjet Power Breaks the Hypersonic Barrier Dryden Lectureship in Research for 2006. In: 44th AIAA Aerospace Sciences Meeting and Exhibit, pp. 1–18. Reno, Nevada, USA (2006). https://doi.org/10.2514/6.2006-1

[5] Hirschel, E. H., Weiland, C.: Design of hypersonic flight vehicles: some lessons from the past and future challenges. *CEAS Space J.* **1**, 3–22 (2011). https://doi.org/10.1007/s12567-010-0004-4

[6] Villace, V.F., Steelant, J.: The Thermal Paradox of Hypersonic Cruisers. In: 20th AIAA International Space Planes and Hypersonic Systems and Technologies Conference, pp. 1–14. Glasgow, Scotland (2015). https://doi.org/10.2514/6.2015-3643

[7] Viola, N., Fusaro, R., Ferretto, D., Gori, O., Saracoglu, B., Ispir, A. C., Schram, C., Grewe, V., Pletzer, J. F., Martinez, J., Marini, M., Hernandez, S., Lammers, K., Vincent, A., Hauglustaine, D., Liebhardt, B., Linke, F., Bodmer, D., Fureby, C., Ibron, C.: H2020 STRATOFLY Project: From Europe to Australia in Less Than 3 Hours. In: 32nd Congress of the International Council of the Aeronautical Sciences (ICAS), pp. 1–21. Shanghai, China (2021)

[8] Bodmer, D., Shah, R., Linke, F., Gollnick, V.: Fuel-efficient flight control design for a hypersonic airliner. In: 70. Deutscher Luft- und Raumfahrtkongress 2021 (DLRK), pp. 1–10. Bremen, Germany (2021). https://www.doi.org/10.25967/550184

[9] Thöben, J., Bodmer, D., Liebhardt, B., Gollnick, V.: Design of Hypersonic Airline Networks with respect to Passenger Demand and Flight Routing. In: 2nd International Conference on High-Speed Vehicle Science & Technology (HiSST), pp. 1–12. Bruges, Belgium (2022)

[10] European Commission: Communication from the Commission to the European Parliament, the Council, the European Economic and Social Committee and the Committee of the Regions: A Roadmap for moving to a competitive low carbon economy in 2050. COM(2011) 112 final. Brussels, Belgium (2011)

[11] European Commission: WHITE PAPER: Roadmap to a Single European Transport Area – Towards a competitive and resource efficient transport system. COM(2011) 144 final. Brussels, Belgium (2011)

[12] European Commission: Flightpath 2050: Europe's Vision for Aviation. Report of the High Level Group on Aviation Research (2011). ISBN-13: 978-92-79-19724-6.

[13] Grewe, V.: Cimate Impact of Hypersonic Aviation. Lecture Series 2021-07 von Karman Institute for Fluid Dynamics (2021)

[14] Liebhardt, B., Lütjens, K., Swaid, M., Müller, M., Ladewich, M.: Sonic Boom Carpet Computation as a Basis for Supersonic Flight Routing. In: AIAA Aviation 2019 Forum, pp. 1–9. Dallas, Texas, USA (2019). https://doi.org/10.2514/6.2019-3387

[15] Federal Aviation Administration: 14 C.F.R §91.817 - Civil aircraft sonic boom (AE 2.106/3:14/). https://www.govinfo.gov/app/details/CFR-2001-title14-vol2/CFR-2001-title14-vol2-sec91-817

[16] Viola, N., Fusaro, R., Gori, O., Marini, M., Roncioni, P., Saccone, G., Saracoglu, B., Ispir, A. C., Fureby, C., Nilsson, T., Ibron, C., Zettervall, N., Nordin Bates, K., Vincent, A., Martinez-Schram, J., Grewe, V., Pletzer, J., Hauglustaine, D., Linke, F., Bodmer, D.: STRATOFLY MR3 – how to reduce environmental impact of high-speed transportation. In: AIAA Scitech 2021 Forum, pp. 1–21. VIRTUAL EVENT (2021). https://doi.org/10.2514/6.2021-1877

[17] Steelant, J., Varvill, R., Defoort, S., Hannemann, K., Marini, M.: Achievements obtained for sustained hypersonic flight within the LAPCAT-II project. In: 20th AIAA International Space Planes and Hypersonic Systems and Technologies Conference, pp. 1–56. Glasgow, Scotland (2015). https://doi.org/10.2514/6.2015-3677

[18] Viola, N., Fusaro, R., Saracoglu, B., Schram, C., Grewe, V., Martinez, J., Marini, M., Hernandez, S., Lammers, K., Vincent, A., Hauglustaine, D., Liebhardt, B., Linke, F., Fureby, C.: Main challenges and goals of the H2020 STRATOFLY project. *Aerotecnica Missili &Spazio*, **100**, 95–110 (2021). https://doi.org/10.1007/s42496-021-00082-6

[19] Linke, F., Grewe, V., Gollnick, V.: The Implications of Intermediate Stop Operations on Aviation Emissions and Climate, Meteorologische Zeitschrift, **26**(6):697–709 (1017). https://doi.org/10.1127/metz/2017/0763

[20] Linke, F.: Trajectory Calculation Module (TCM) - Tool Description and Validation. DLR internal report IB-328-2009-01. German Aerospace Center, Institute of Air Transportation Systems, Hamburg, Germany (2009)

[21] Bodmer, D.: Flugmechanische Bewegungsgleichungen für Hyperschallflugzeuge unter Berücksichtigung der Erdkrümmung und -rotation. ILT internal report IB-M28-2023-23. Hamburg University of Technology (TUHH), Institute of Air Transportation Systems (ILT), Hamburg, Germany (2023)

[22] N. N.: U.S. Standard Atmosphere 1976. Washington D.C, National Oceanic and Atmospheric Administration, National Aeronautics and Space Administration (1976)

[23] Saracoglu, B. H., Ispir, A. C., Hurtig, T.: Propulsion Subsystems design. Technical Report WP 2.4, GA-769246 STRATOFLY, Ref. Ares(2021)5976248. Sint-Genesius-Rode, Belgium (2021)

[24] Natale, P., Cutrone, L., Roncioni, P.: CFD Simulations for Combustor Optimization. Technical Report WP 3.3, GA-769246 STRATOFLY, Ref. Ares(2021)5745339. Capua, Italy (2021)

[25] Voshell, M.: High Acceleration and the Human Body. http://csel.eng.ohio-state.edu/voshell/gforce.pdf - assessed on 13 February 2024.

[26] Brockhaus, R., Alles, W., Luckner, R.: Flugregelung. Springer-Verlag Berlin Heidelberg, 3. Edition (2011). ISBN-13: 978-3-642-01443-7

[27] Saccone, G., Ispir, A. C., Saracoglu, B. H., Cutrone, L., Marini, M.: Computational evaluations of emissions indexes released by the STRATOFLY air-breathing combined propulsive system. *Aircraft Engineering and Aerospace Technology*, **94**(9):1499-1507 (2022). https://doi.org/10.1108/AEAT-01-2022-0024

[28] Cutrone, L., Saccone, G., Martinez, J., Luis, D., Vincent-Randonnier, A., Nilsson, T., Fureby, C., Ibron, C., Zettervall, N., Nordin-Bates, K., Bodmer, D., Weder, C. M.: Emissions and emission reduction potentials. Technical report WP 4.1, GA-769246 STRATOFLY, Ref. Ares(2021)5771857. Capua, Italy (2021)

[29] Maglieri, D. J., Bobbitt, P. J., Plotkin, K. J., Shepherd, K. P., Coen, P. G., Richwine, D. M.: Sonic Boom - Six Decades of Research. NASA SP-2014-622. Langley Research Center. Hampton, Virgina (2014)

[30] Qiao, J.-L., Han, Z., Song, W., Song, B.-F.: Development of Sonic Boom Prediction Code for Supersonic Transports Based on Augmented Burgers Equation. In: AIAA Aviation 2019 Forum, pp. 1–19. Dallas, Texas, USA (2019). https://doi.org/10.2514/6.2019-3571

[31] Chavas, D.: land_or_ocean.m, MATLAB Central File Exchange. https://www.mathworks.com/matlabcentral/fileexchange/45268-land_or_ocean-m, Retrieved February 18, 2024.

[32] Ingenito, A.: Impact of hydrogen fueled hypersonic airliners on the O3 layer depletion, *International Journal of Hydrogen Energy*, **43**(50):22694-22704 (2018). https://doi.org/10.1016/j.ijhydene.2018.09.208

